ACS Photonics

Article

pubs.acs.org/journal/apchd5

Enhanced Photon Collection in Luminescent Solar Concentrators with Distributed Bragg Reflectors

Lu Xu,[†,⊥] Yuan Yao,[†,⊥] Noah D. Bronstein,[‡] Lanfang Li,[†] A. Paul Alivisatos,[∥,‡,§] and Ralph G. Nuzzo*[,†]

[†]Department of Chemistry, Frederick Seitz Materials Research Laboratory, University of Illinois at Urbana−Champaign, Urbana, Illinois 61801, United States

[∥]Department of Materials Science and Engineering, Kavli Energy NanoScience Institute, University of California, Berkeley, California 94720, United States

[‡]Department of Chemistry, University of California, Berkeley, California 94720, United States

[§]Materials Science Division, Lawrence Berkeley National Laboratory, Berkeley, California 94720, United States

Supporting Information

ABSTRACT: Escape cone loss is one of the primary limiting factors for efficient photon collection in large-area luminescent solar concentrators (LSCs). The Stokes shift of the luminophore, however, opens up an opportunity to recycle the escaped luminescence at the LSC front surface by utilizing a photonic band-stop filter that reflects photons in the luminophore's emission range while transmitting those in its absorption range. In this study, we examine the functional attributes of such photonic filter designs, ones realized here in the form of a distributed Bragg reflector (DBR) fabricated by spin-coating alternating layers of SiO_2 and SnO_2 nanoparticle suspensions onto a supportive glass substrate. The central wavelength and the width of the photonic stopband were programmatically tuned by changing the layer thickness and the refractive index contrast between the two dielectric materials. We explore the design sensitivities for a DBR with an optimized stopband frequency that can effectively act as a top angle-restricting optical element for a microcell-based LSC device, affording further capacities to boost the current output of a coupled photovoltaic cell. Detailed studies of the optical interactions between the photonic filter and the LSC using both experimental and computational approaches establish the requirements for optimum photon collection efficiencies.

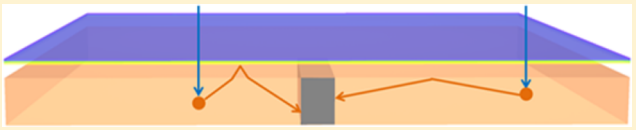

KEYWORDS: *luminescent solar concentrator, distributed Bragg reflector, photovoltaics, escape cone loss*

The concept of photovoltaic (PV) technologies exploiting luminescent solar concentrators (LSCs) has been studied since the 1970s.[1,2] These devices utilize a fluorescent material to absorb the incident illumination and emit lower-energy photons into confined modes within a polymer waveguide, which can then be redirected to an attached solar cell via total internal reflection (TIR). The principal advantages of an LSC are that it operates independent of the incident irradiance angle, collects both direct and diffuse sunlight, and thus eliminates the need for precise mechanical tracking required by a geometric solar concentrator (GSC). The intention for an LSC is to replace expensive active PV materials with relatively inexpensive luminophores.[3−5] Recent reports from our group illustrate an unconventional geometry for LSCs whereby arrays of silicon- or GaAs-based solar microcells (μ-cells) are directly embedded in a much thinner (~30 μm) polymer matrix doped with organic or inorganic luminophores.[6−8] In this LSC system, the sidewalls and bottoms of the μ-cells are utilized to capture the luminescence, while the top surfaces absorb the direct sunlight. A key feature of this layout is the large geometric gain achieved within a relatively small waveguide area due to the small dimensions of the semiconductor device. The prospective cost-effectiveness of this design follows from the low semiconductor material consumption of these lightweight devices and the capability of optimizing device spacing *via* a transfer-printing process.[9]

The achievable concentration ratios and efficiencies of LSC devices have been limited historically by several loss mechanisms, including (1) incomplete absorption of the incident illumination due to the limited spectral coverage of the luminophore; (2) a portion of absorbed photons not being reemitted, as the quantum yield (QY) of most dyes are typically less than unity; and (3) a portion of the emitted light being refracted out of the waveguide through an escape cone rather than being trapped inside it via TIR.[10,11] In addition, for luminophores with an absorption/emission band overlap, emitted photons in the TIR mode can be reabsorbed by adjacent luminescent molecules, further increasing their chances of being lost via the above-mentioned mechanisms (2) and (3).[12] These features have been discussed in earlier reports from leading research groups.[8,13−17] The current work addresses in great detail one of these issues, escape cone losses, to establish quantitative guidance for designs we have described for its mitigation.[18]

Received: November 4, 2015
Published: January 7, 2016

DOI: 10.1021/acsphotonics.5b00630
ACS Photonics 2016, 3, 278−285

Escape cone loss is one of the primary limiting factors for large LSC devices. As illustrated in Figure 1, all emitted photons impinging on the internal surface with an angle smaller than the critical angle leave the waveguide and are lost. The trapping efficiency (η) in this process is determined by the refractive index of the waveguide (n):

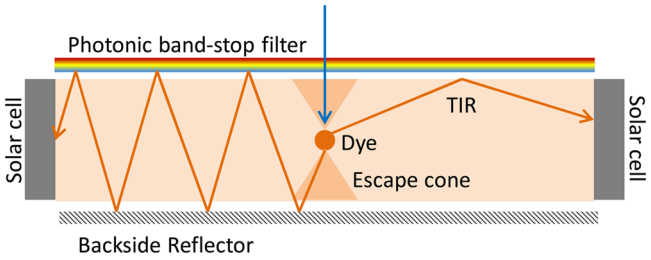

Figure 1. Effects of a photonic band-stop filter on top of an LSC device: the filter selectively reflects back luminesced photons in non-TIR modes and guides them to the attached solar cell to generate extra power, while allowing the transmission of light in the dye absorption range.

$$\eta = \sqrt{1 - n^{-2}} \quad (1)$$

For a typical organic polymeric material as an example (n = 1.5), η is around 74%, which means that 26% of the emitted photons are lost through the front and back surfaces.[19] An attached backside reflector (BSR) does not change this number, as photons still leave the LSC through the front surface after being reflected at the backside. However, the Stokes shift between the dye absorption and emission spectra opens up an opportunity to trap all of the potentially escaping photons at the front surface using a photonic band-stop filter, which reflects all the light in the dye emission range while transmitting all the light in the absorption range (see Figure 1).[20,21] Such an idealized filter would eliminate the escape cone losses completely. A real filter, however, will show a reduced performance for several reasons. First, as an absorption/emission overlap exists in all dye species, it is impossible to design a filter that reflects all the emitted luminescence without some measure of losses in the luminophore's absorption band. Second, the reflectivity of the filter's stopband will be lower than unity, and so not all light in the escape cone will be recycled. Finally, the most important challenge with a photonic band-stop filter originates from the dependence of reflectance on the photon incidence angle. The stopband typically is shifted toward shorter wavelengths, with a decreasing reflectivity seen for increasing incidence angles. As the directions of the luminescent photons impinging on the front surface of the LSC are isotropic, photons with oblique angles are subjected to a lower trapping efficiency with a photonic mirror as compared to ones with a steeper angle of incidence. Light with steep angles, however, results in extremely long effective path lengths within the waveguide before it reaches the solar cell. It therefore suffers more strongly from path-length-dependent losses, including dye reabsorption, matrix absorption, and scattering. As a consequence, the photon recycling efficiency of the top filter will be dependent on the photon incidence angles, a result of both the filter's angle-dependent reflectivity and the path-length-dependent propagation losses.

These complexities make the demands placed on the quality of the photonic structure very high.[22] Only a filter with very low reflectance in the absorption range of the dye, a very high reflection in the emission range, and a very steep edge between these two spectral ranges has the potential to produce large/useful increases in light collection efficiency. The bandwidth and central wavelength of the filter further therefore need to be carefully designed to overcome the angle dependence of the reflectance and the resulting path-length-dependent loss of recycled photons. Suitable candidates for such structures include organic cholesteric mirrors,[23−26] inorganic Bragg stacks,[27−30] and rugate filters.[31−35] These optical structures are all one-dimensional photonic crystals, consisting of alternating layers of two materials with a refractive index contrast. The reflected waves at each layer boundary can interfere constructively, creating high reflectance for a certain wavelength range, the so-called photonic stopband. These photonic structures have been used as band-stop filters directly on solar cells[36] and LSCs[37−40] to selectively reflect photons within the escape cone and to achieve enhanced photon recycling. In a recent report from our group, we described an LSC design utilizing core−shell quantum dots combined with a photonic mirror that reflects the entire narrow emission band at nearly all angles, achieving a concentration ratio exceeding 30 for blue photons.[18]

In this study, we examine in quantitative form the design sensitivities for the improvements realized in the power output of the Si microcell-based LSC system by incorporating a top photonic mirror, which serves as an angle-restricting optical element that traps luminescence that would otherwise be lost. The model photonic structure was realized by fabricating a distributed Bragg reflector (DBR) that consists of alternating layers of suspensions of spin-coated SiO_2 and SnO_2 nanoparticles. The position and the width of its photonic stopband can be effectively tuned by the layer thickness and the refractive index contrast between the two dielectric materials. The versatility of this fabrication process allowed us to systematically study the light management effects of the DBR on an LSC device by employing a series of DBRs with different central wavelengths (λ_c). The stopbands of these mirrors were tuned to be relatively narrow compared to our previous work, so that the recycling behavior for the emitted photons at different angles could be examined. The luminophore chosen in this study is an organic dye (4-(dicyanomethylene)-2-methyl-6-(*p*-dimethylaminostyryl)-4*H*-pyran, DCM) instead of quantum dots, as it enables us to better study the optical physics related to escape cone losses by generating LSC waveguides at high optical densities with minimum scattering. Our experimental results show that the optimal λ_c is the one that is red-shifted from the emission peak. For the LSC studies reported here for a microcell incorporating a diffuse backside reflector, adding the best-performing DBR results in a marked (23%) relative enhancement in the photocurrent generated from the luminophores. The detailed mechanism of the photon recycling process between DBR and LSC is elucidated by the results of spectrum-resolved quantum efficiency measurements. In addition, a Monte Carlo ray-tracing simulation was developed to capture the photon traveling behavior and further understand the characteristics of light propagation inside the waveguide.

FABRICATION AND OPTICAL PROPERTIES OF THE DBR

A series of DBRs with different λ_c values were fabricated via layer-by-layer spin-coating of SiO_2 and SnO_2 nanoparticle suspensions with a subsequent calcination step to remove

DOI: 10.1021/acsphotonics.5b00630
ACS Photonics 2016, 3, 278−285

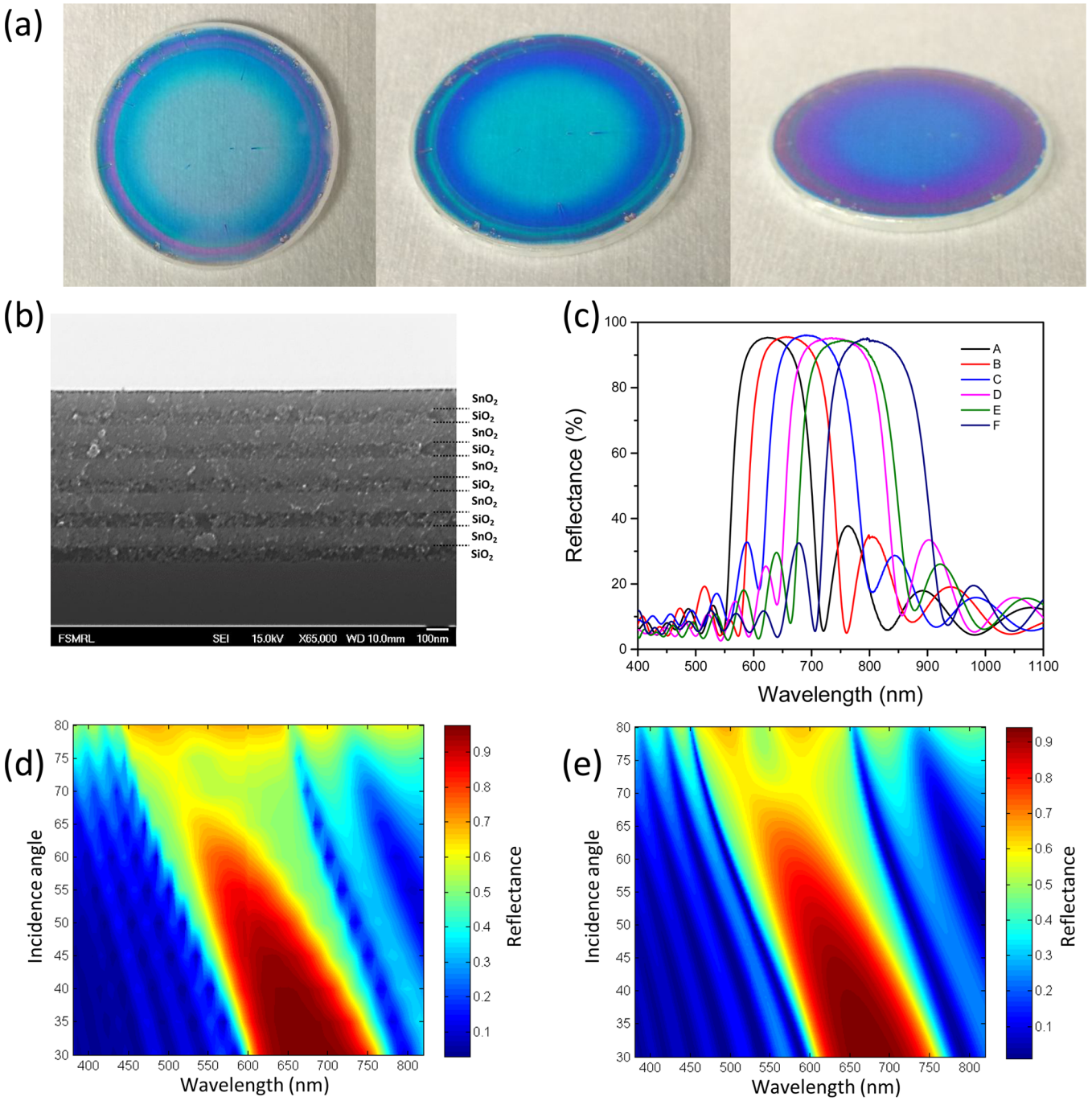

Figure 2. Characterization of fabricated photonic structure. (a) Optical images of a spin-coated DBR. Its central region shifts from blue to purple as the viewing angles become more oblique. (b) Cross-sectional SEM image of a DBR with alternating layers of SiO_2 and SnO_2. (c) Reflectance (normal incidence) of six DBRs with various stopband positions, achieved by tuning the thickness of the spin-coated dielectric layer. (d) Experimental and (e) simulated reflectance spectra of a DBR. Its stopband shifts to shorter wavelength range with increasing incidence angles.

residual organic components, as reported by Puzzo et al.[41] The as-prepared dielectric multilayer, here supported on a quartz substrate, displays high optical uniformity over a large central region of the optic, with minimal adventitious defects, as illustrated by the optical images presented in Figure 2a. It is noteworthy that the size of the DBR is only limited by that of the underlying substrate and could be expanded by using a larger quartz plate and optimized coating processes. A cross-sectional secondary electron microscopy (SEM) image of the fabricated DBR is presented in Figure 2b. The spin-coating method yields a periodic multilayer stack with well-defined, flat interfaces between the adjacent layers, which are critical to minimize undesired scattering/refraction and ensure excellent optical properties. The first-order stopband central wavelength (λ_c) of the DBR is determined by the Bragg equation:

$$\lambda_c = 2(n_1 d_1 + n_2 d_2) \quad (2)$$

where n_1 and d_1 and n_2 and d_2 are the refractive indices and thicknesses of the two dielectric materials in the stack, respectively. In this fabrication protocol, the thickness of each dielectric layer can be effectively manipulated via the spin-coating speed and suspension concentration (see Figure S1),

DOI: 10.1021/acsphotonics.5b00630
ACS Photonics 2016, 3, 278−285

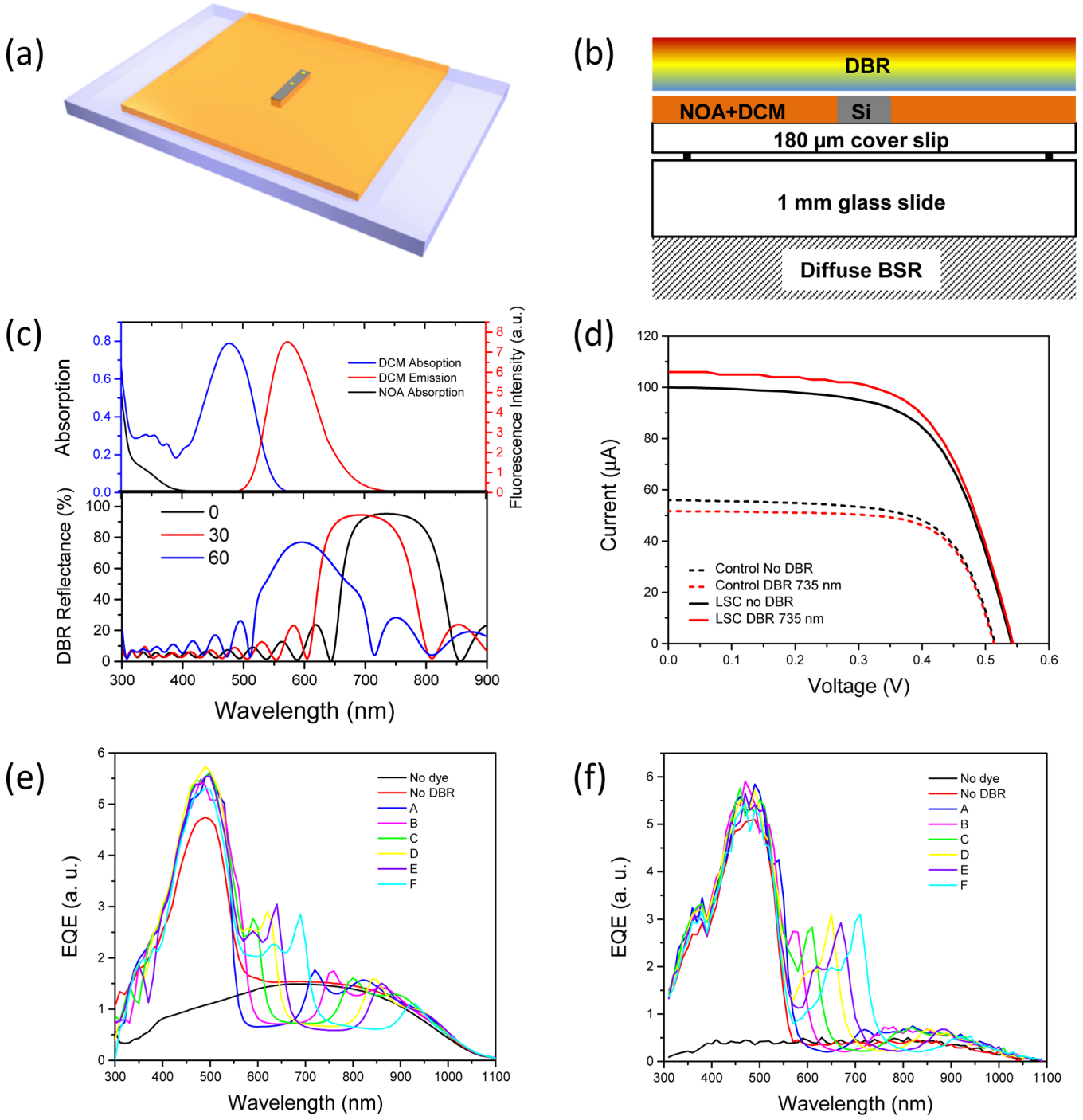

Figure 3. (a) 3D illustration of an LSC device composed of a silicon solar microcell (gray) and a polymer matrix doped with DCM (orange) supported on a thin glass substrate (light lavender). (b) Cross-sectional schematic of the LSC device with a top DBR. (c) Comparison between DCM absorption/emission spectra and DBR reflectance. A DBR allows the transmission of dye emission at close to normal incidence, while it reflects dye emission at larger incidence angles. (d) I–V curves. Adding a DBR on top results in an increase of I_{sc} for an LSC device. (e) Experimental and (f) simulated EQE for an LSC device with various DBRs. The photon recycling effects are evidenced by the enhancements in the blue region.

generating DBRs with various values of λ_c. The reflectance spectra of the as-prepared DBRs were measured at normal incidence and are plotted in Figure 2c. The experimental spectra agree well with ones simulated using the transfer-matrix method (see Figure S2), confirming the high optical quality of the DBRs. The reflectivity of a DBR increases with the number of alternating layers, owning to the increasing number of constructive and destructive interferences occurring at its layer boundaries. Each DBR for which data are presented in Figure 2c consists of 16 alternating layers, leading to peak reflectance values as high as 95%. These values are suitable for use in studies exploring their utility as photonic band-stop filters for LSCs. The stopbands of the DBR shift to shorter wavelengths as the light incidence angles (θ) increase, as shown by the experimental and simulated reflectance data presented in Figure 2d and e. This effect can be seen visually by looking at the DBR

DOI: 10.1021/acsphotonics.5b00630
ACS Photonics 2016, 3, 278–285

at different viewing angles (Figure 2a). The angle-dependent reflectance of the DBR provides a critical constraint for the design of an LSC-DBR system, as an optimized DBR should allow high optical transmission in the dye absorption range while providing angle restriction for escaped luminescence, as discussed in greater detail in sections that follow.

PERFORMANCE OF AN LSC WITH A DBR ON TOP

The LSC system utilized in this study consists of transfer-printed silicon solar microcells[42] (30 μm thick, 100 μm wide, and 1.5 mm long) embedded in a polymer matrix doped with an organic luminophore (DCM), supported on a thin (180 μm thick) quartz substrate, as illustrated in Figure 3a.[8] An embedded PV microcell provides what is an essentially weakly perturbing means for measuring the photon fluxes present in the waveguide. A DBR (λ_c = 735 nm, sample D in Figure 2c) is placed directly on top of the LSC device with a natural air gap in-between to trap the escaped luminescence, while photons already in the TIR modes remain unaffected by the photonic structure (a cross-sectional illustration is presented in Figure 3b). This particular photonic mirror is designed to allow high transmission of incident illumination within the DCM absorption range, while providing high reflectance for emitted luminescence at larger incidence angles. This can be seen in the comparison of the dye absorption/emission spectra and the DBR reflectance data presented in Figure 3c: it is notable that the DBR reflectance peak matches that of the dye emission when θ = 60 degrees (i.e., not at normal incidence). The relationship between dye emission and stopband frequencies in terms of the LSC performance is discussed further in the following section. With the addition of the DBR (λ_c = 735 nm), the short circuit current (I_{sc}) of the device increased 6%, from 100 μA to 106 μA (Figure 3d). In contrast, the I_{sc} of the blank control sample (no luminophore in the polymer matrix) dropped from 56.0 μA to 51.8 μA after applying the DBR, due to the fact that the DBR stopband blocks part of the incoming solar radiation that can be utilized by the microcell through non-TIR waveguiding. To isolate the luminescence recycling effects from the top photonic structure, the current output contributed from the dye emssion (I_{dye}) was calculated by subtracting the I_{sc} of the blank control sample. Compared with the LSC value without a DBR (I_{dye} = 100−56 = 44 μA), the I_{dye} value (106−51.8 = 54.2 μA) of an LSC with a DBR showed a 23% relative enhancement, indicating that otherwise escaping photons are being recycled back into the waveguide by the top photonic mirror.

The light management properties of the different DBRs were further elucidated by the results of the external quantum efficiency (EQE) measurements, the data for which are presented in Figure 3e. The benefits from the luminophore on PV performance are highlighted by the marked blue spectrum enhancements that are seen, ones corresponding to the dye absorption (curves in red vs black in Figure 3e). This illustrates the changing fraction of the emitted photons from the luminophore that are trapped in TIR modes and subsequently collected by the embedded solar cell in the waveguide. The DBR series A−F (reflectance data shown in Figure 2c) were placed directly on top of the LSC device. Adding photonic band-stop filters results in a significant dip in the EQE curves at frequencies corresponding to their photonic stopbands. This effect is also seen in the EQE measurements made of a blank control sample without a luminophore present when the same DBRs are applied on top (Figure S3). These results show that the photonic filter brings intrinsic challenges in that it blocks the part of the solar spectrum corresponding to its stop-bandwidth. This blocking of illumination results in a decrease in the short-circuit current. This negative effect can be mitigated, however, by reducing the bandwidth of the DBR, with the caveat that a lessened coverage of the dye emission spectrum will lead to a lowered luminescent photon trapping efficiency. The key point is that, for an overall positive effect, the illumination blocking loss will need to be exceeded by the current gain from the photon recycling afforded by the DBR. Experimentally, the enhanced EQE responses seen after adding a DBR are observed at two distinctive regions (Figure 3e): the first occurring on the high-energy side of the DBR stopbands (580 to 700 nm) and the second in the dye absorption region (300 to 580 nm).

The features seen on the high-energy side of the stopbands in the EQE plots are due to the angle restriction effects of the DBR on the photons reflected by the diffuse backside reflector. Here the photons transmitted through the LSC film bounce back with randomized directions and, when they reach the top photonic mirror again, have new, angular-dependent chances of being recycled into propagating modes (non-TIR) inside the cavity between the DBR and diffuse backside reflector before reaching the cell. Since the DBR reflectance blue-shifts as the incident angle increases, photons with a higher energy than the DBR band gap have a larger chance of being recycled, leading to enhanced collection efficiencies on this side of the stopband. It is important to note that this enhancement is not large enough to compensate for the total current loss due to the stopband, a conclusion further supported by the fact that all current output from a blank control sample (i.e., without luminophore) decreases when it was coupled with a DBR (Figure S3).

Significant UV-blue region enhancements associated with dye absorption are observed with all the DBRs (Figure 3e), as each can reflect fluorescent photons within a certain range of incident angles. As its stopband red-shifts away from the dye emission peak, the photons that can be reflected by the DBR will be at a larger angle of incidence. For example, the reflectance of DBR A (λ_c = 620 nm) matches the dye emission at an angle close to normal incidence, while for DBR D (λ_c = 735 nm), matches it at around 60 degrees (Figure 3c). To assess the quantitative impacts of these effects, an integration of the EQE with excitation by the AM 1.5G solar spectrum was carried out between 300 and 580 nm (the dye absorption range) to quantify the current contribution coming from the dye luminescence for each of the different DBRs. These results are presented in Table 1.

As is shown by these data, DBRs B to E have similar current outputs in this particular spectral region as compared to the control sample (see Table 1 for ΔI values, defined as the difference between the samples with and without a DBR), where sample D performs the best, showing a relative

Table 1. Calculated Current Contributed by Photons in the DCM Absorption Range

	λ_c (nm)						
	no DBR	620 (A)	656 (B)	690 (C)	735 (D)	760 (E)	800 (F)
$I_{300-580}$ (μA)	52.9	57.6	63.0	63.6	64.4	61.9	58.7
ΔI (μA)	0	4.8	10.1	10.8	11.5	9.1	5.8

DOI: 10.1021/acsphotonics.5b00630
ACS Photonics 2016, 3, 278−285

enhancement of ~22%. For DBR A, the enhancement is the lowest, as its stopband blocks the low-energy side of the absorption edge of the DCM dye. Its angle restriction property further limits its efficiency, being subject to higher path-length-dependent losses. The properties of DBR F are also limited for reasons that fall at the other limit. Here, the stopband red shift is too large to cover the dye emission effectively, even at very large incidence angles. As a result the DBR reflectance drops significantly at oblique angles, which leads to a low photon recycling efficiency. To extend understandings of these optical effects, a Monte Carlo ray-tracing model was constructed using measured material optical constants, with the reflectance for each DBR being calculated using the transfer-matrix method. All of the features observed in the experimental EQE plots (Figure 3e)—stopband dips, diffuse light enhancements, and the UV-blue region enhancements—are also well captured in the simulated EQE curves, as shown in the data presented in Figure 3f.

The results of measurements of the total current output from the LSC device with each DBR are plotted in Figure 4a (black dots and line). The optimum system among these DBRs is that afforded by sample D, with a central wavelength of 735 nm. From these data it is clear that the center wavelength of the DBR needs to be red-shifted substantially from the dye emission peak (600 nm) for best performance. For sample D, the DBR stopband fully overlaps with dye emission at around 60 degree incidence angles (Figure 3c), indicating that the design of the photonic structure's stopband should target photons in this range as they have the highest chance of being guided to the cell. The Monte Carlo ray-tracing simulations affirm this interpretation. The results of simulations addressed to this point are shown plotted against the experimental data in Figure 4a (blue curve). The agreement in the general trend versus DBR central wavelength confirms the inferred trends in the efficacy of enhanced light trapping of the LSC system. These results thus provide and affirm a theoretical guideline for designing a DBR with respect to the dye emission profile of the LSC. The relative current enhancements integrated from the dye absorption range (300−580 nm) in EQE plots are plotted in Figure 4b, demonstrating a similar trend to Figure 4a, and further confirm the relationship between DBR center wavelength and device current enhancement.

In order to investigate light propagation behavior inside the LSC film, the device performance was also measured with a circular aperture centered on the solar cell while controlling the illumination area of the LSC device with DBR D affixed on top. The photocurrents extracted from these measurements are plotted as a function of aperture radius in Figure 4c. At smaller aperture radii, the LSC without the DBR (black curve) performs better, as the stopband of the top photonic structure blocks incident light that can be waveguided to the device via non-TIR modes within short ranges.[42] The DBR-LSC coupled device (red curve) exhibits a faster growth rate in the current output as the aperture area expands, outperforming the control device at larger radii. This indicates that a longer propagation distance of luminescent photons occurs inside the waveguide with a top photonic mirror being affixed and, thus, illustrates a beneficial role for their use in improving performance in large LSC devices.

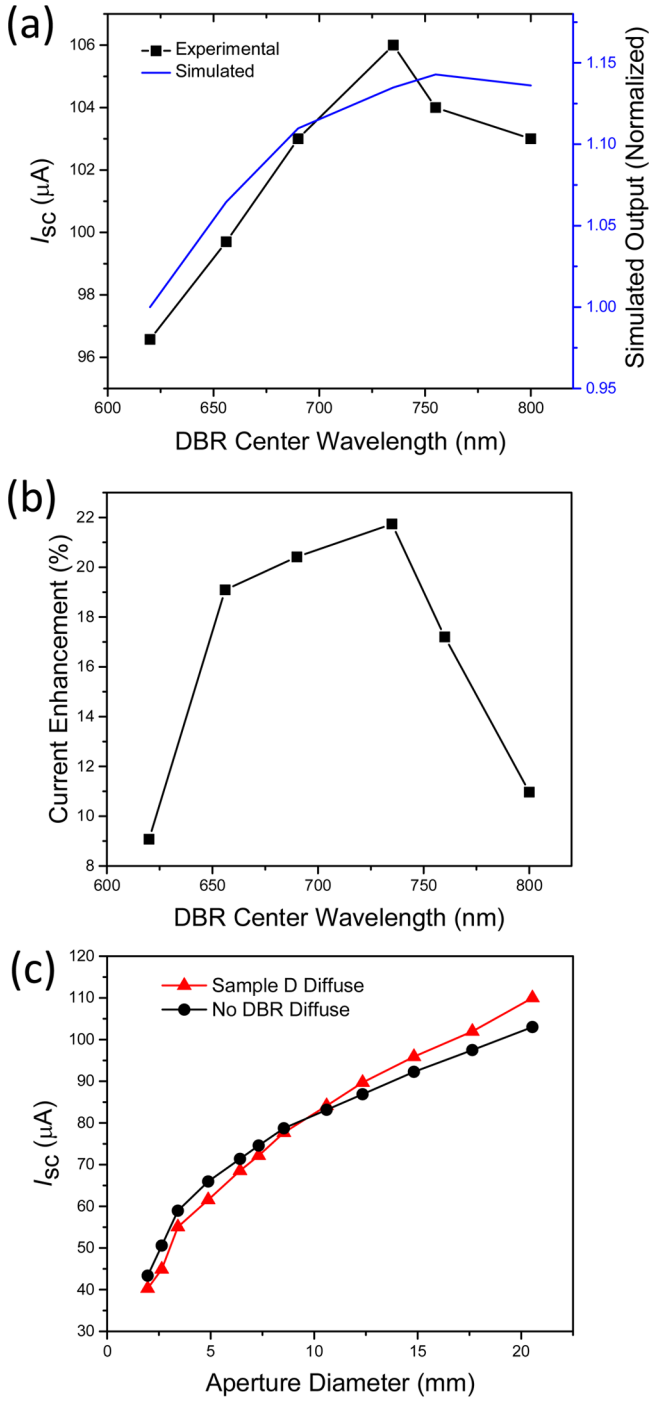

Figure 4. (a) Both experimental and simulated enhancements show that the optimal stopband of the DBR red-shifts from the dye emission peak. (b) Relative current enhancements integrated from the dye absorption range (300 to 580 nm) in the EQE plots. The DBR with a center wavelength of 735 nm shows the best performance. (c) An LSC with a DBR shows a faster increase in current output with increasing illumination area, indicating a longer photon propagation length.

CONCLUSION

The design-rule-dependent light management effects of DBR photonic structures on a microcell-based LSC device are demonstrated by both $I-V$ and EQE measurements, where the best DBR results in a marked 23% current enhancement generated from the dye emission. The spectral response measurement maps out the enhancement for emitted photon and diffuse photons, as well as the blocking of illumination within the DBR stopband. Comparing the experimental data from different DBRs, we found that the center wavelength of

DOI: 10.1021/acsphotonics.5b00630
ACS Photonics 2016, 3, 278−285

the DBR needs to be red-shifted significantly from the dye emission peak for optimal performance. These results show good agreement with Monte Carlo ray-tracing simulations. Finally, we have shown that the photons in the LSC with a top photonic mirror possess a longer propagation distance, confirming the photon recycling effects that result from the angle-restricted reflectance.

There exist many opportunities to improve performance in this design, and we have shown in our own work the important improvement that attends careful design of the luminophore.[8,12] It is also possible to use a transfer-assembly process with other solid inks, including III−V devices (e.g., InGaP) with larger band gaps that could potentially minimize the stopband loss observed here with a silicon device. Thus, using a luminophore with a larger Stokes shift and narrower emission bandwidth (such as obtained with core−shell quantum dots or quantum rods)[18,43,44] and selective, omnidirectional (e.g., metasurface) reflectors could potentially lead to much higher photon recycling and conversion efficiencies for LSC-based solar concentrators.

METHODS

SiO_2 and SnO_2 nanoparticles were purchased from Sigma-Aldrich (Ludox SM-30, 30 wt %) and Nyacol Inc. (15 wt %), respectively. A SiO_2 suspension was diluted to the desired concentration. Each suspension was filtered through a 2 μm pore syringe filter to remove any nanoparticle agglomerates. Piranha-cleaned quartz discs or silicon wafers were used as substrates for the nanoparticle DBRs. The prepared SiO_2 and SnO_2 nanoparticle suspension was spin-coated sequentially onto the substrate between 2000 and 5000 rpm for 30 s until 16 layers were deposited. Following each layer deposition, the substrate was baked on a hot plate at 400 °C for 30 min. A small opening the size of the solar cell was carved in the center of the DBR with a razor blade to allow direct solar radiation on the top surface of the cell.

Fabrication of an LSC Integrated with a Si Solar Microcell. Fabrication and transfer-printing of solar microcells have been described previously. A glass substrate is prepared by spin-coating a layer of partially cured UV-curable adhesive (NOA61, Norland) at 3000 rpm. Then 30 μm soda lime glass beads (SPI product #2714) were sparsely sprinkled onto the four corners of the substrate. A repel silane (GE Health)-treated quartz plate was then secured on top of the printed cell module. A solution of DCM in NOA was then capillary-filled into the cavity with the flow parallel to the long axis of the microcell. The assembly was cured for 20 min under UV light, and the quartz top plate was peeled off afterward. The top contact of the device was achieved by screen-printing a silver epoxy (E4110, Epoxy Technology) line on two top contacts of the cell and curing at room temperature for 48 h. The DBR was directly applied on top of the LSC device with the solar cell aligned with the carved opening in the middle of the DBR. The control sample was measured with a quartz plate the same as the DBR substrate applied on top to compensate for the reflectance of the quartz plate surface.

SEM images were obtained on a JEOL 7000 FE scanning electron microscope. Film thickness and angle-resolved reflectance of the DBR were measured using a J.A. Woollam VASE ellipsometer. Photovoltaic characterization was performed with a Keithley 2400 sourcemeter. The illumination source was an Oriel 91192-1000W solar simulator with an AM1.5G filter. Its light intensity was calibrated to one sun and monitored by a radiant power meter and probe (New Port 70260 and 70268), with a measured intensity fluctuation of ∼1%. External quantum efficiency was measured using a Gooch & Housego OL-750 automated spectroradiometric system.

Monte Carlo ray-tracing simulation code was written in a MATLAB program. The geometry was simulated the same as the experimental device. Luminescence, scattering, and reflection were all treated probabilistically with a random number generator by the program. The polarization of the photon was set at 45 deg for all incoming photons and is subject to change when scattering or luminescence occurs. Reflection and refraction were calculated with Fresnel equations, assuming the refractive index of the glass was 1.5 and the NOA was 1.56 at all wavelengths. The absorption probability of each photon in the solar cell was calculated with the external quantum efficiency measurement result with the bare silicon solar cell.

ASSOCIATED CONTENT

Supporting Information

The Supporting Information is available free of charge on the ACS Publications website at DOI: 10.1021/acsphotonics.5b00630.

Spin-coat recipe for nanoparticles, simulated reflectance of DBRs, and effect of DBRs on a blank control sample (PDF)

AUTHOR INFORMATION

Corresponding Author

*E-mail: r-nuzzo@illinois.edu.

Author Contributions

⊥L. Xu and Y. Yao contributed equally to this work.

Notes

The authors declare no competing financial interest.

ACKNOWLEDGMENTS

This work was supported by the "Light-Material Interactions in Energy Conversion" Energy Frontier Research Center funded by the U.S. Department of Energy, Office of Science, Office of Basic Energy Sciences, under Award Number DE-SC0001293.

REFERENCES

(1) Weber, W. H.; Lambe, J. Luminescent greenhouse collector for solar radiation. *Appl. Opt.* **1976**, *15*, 2299−2300.

(2) Goetzberger, A.; Greube, W. Solar energy conversion with fluorescent collectors. *Appl. Phys.* **1977**, *14*, 123−139.

(3) Hermann, A. M. Luminescent solar concentrators—A review. *Sol. Energy* **1982**, *29*, 323−329.

(4) Debije, M. G.; Verbunt, P. P. C. Thirty Years of Luminescent Solar Concentrator Research: Solar Energy for the Built Environment. *Adv. Energy Mater.* **2012**, *2*, 12−35.

(5) Reisfeld, R.; Shamrakov, D.; Jorgensen, C. Photostable solar concentrators based on fluorescent glass films. *Sol. Energy Mater. Sol. Cells* **1994**, *33*, 417−427.

(6) Yoon, J.; Li, L.; Semichaevsky, A. V.; Ryu, J. H.; Johnson, H. T.; Nuzzo, R. G.; Rogers, J. A. Flexible concentrator photovoltaics based on microscale silicon solar cells embedded in luminescent waveguides. *Nat. Commun.* **2011**, *2*, 343.

(7) Sheng, X.; Shen, L.; Kim, T.; Li, L.; Wang, X.; Dowdy, R.; Froeter, P.; Shigeta, K.; Li, X.; Nuzzo, R. G.; Giebink, N. C.; Rogers, J. A. Doubling the Power Output of Bifacial Thin-Film GaAs Solar Cells by Embedding Them in Luminescent Waveguides. *Adv. Energy Mater.* **2013**, *3*, 991−996.

DOI: 10.1021/acsphotonics.5b00630
ACS Photonics 2016, 3, 278−285

(8) Bronstein, N. D.; Li, L.; Xu, L.; Yao, Y.; Ferry, V. E.; Alivisatos, A. P.; Nuzzo, R. G. Luminescent Solar Concentration with Semiconductor Nanorods and Transfer-Printed Micro-Silicon Solar Cells. *ACS Nano* **2013**, *8*, 44−53.
(9) Yoon, J.; Baca, A. J.; Park, S.-I.; Elvikis, P.; Geddes, J. B.; Li, L.; Kim, R. H.; Xiao, J.; Wang, S.; Kim, T.-H.; Motala, M. J.; Ahn, B. Y.; Duoss, E. B.; Lewis, J. A.; Nuzzo, R. G.; Ferreira, P. M.; Huang, Y.; Rockett, A.; Rogers, J. A. Ultrathin silicon solar microcells for semitransparent, mechanically flexible and microconcentrator module designs. *Nat. Mater.* **2008**, *7*, 907−915.
(10) McDowall, S.; Butler, T.; Bain, E.; Scharnhorst, K.; Patrick, D. Comprehensive analysis of escape-cone losses from luminescent waveguides. *Appl. Opt.* **2013**, *52*, 1230−1239.
(11) Peters, M.; Goldschmidt, J. C.; Löper, P.; Bläsi, B.; Gombert, A. The effect of photonic structures on the light guiding efficiency of fluorescent concentrators. *J. Appl. Phys.* **2009**, *105*, 014909.
(12) Giebink, N. C.; Wiederrecht, G. P.; Wasielewski, M. R. Resonance-shifting to circumvent reabsorption loss in luminescent solar concentrators. *Nat. Photonics* **2011**, *5*, 694−701.
(13) Erickson, C. S.; Bradshaw, L. R.; McDowall, S.; Gilbertson, J. D.; Gamelin, D. R.; Patrick, D. L. Zero-Reabsorption Doped-Nanocrystal Luminescent Solar Concentrators. *ACS Nano* **2014**, *8*, 3461−3467.
(14) Meinardi, F.; Colombo, A.; Velizhanin, K. A.; Simonutti, R.; Lorenzon, M.; Beverina, L.; Viswanatha, R.; Klimov, V. I.; Brovelli, S. Large-area luminescent solar concentrators based on 'Stokes-shift-engineered' nanocrystals in a mass-polymerized PMMA matrix. *Nat. Photonics* **2014**, *8*, 392−399.
(15) Coropceanu, I.; Bawendi, M. G. Core/Shell Quantum Dot Based Luminescent Solar Concentrators with Reduced Reabsorption and Enhanced Efficiency. *Nano Lett.* **2014**, *14*, 4097−4101.
(16) Bradshaw, L. R.; Knowles, K. E.; McDowall, S.; Gamelin, D. R. Nanocrystals for Luminescent Solar Concentrators. *Nano Lett.* **2015**, *15*, 1315−1323.
(17) Meinardi, F.; McDaniel, H.; Carulli, F.; Colombo, A.; Velizhanin, K. A.; Makarov, N. S.; Simonutti, R.; Klimov, V. I.; Brovelli, S. Highly efficient large-area colourless luminescent solar concentrators using heavy-metal-free colloidal quantum dots. *Nat. Nanotechnol.* **2015**, *10*, 878−885.
(18) Bronstein, N. D.; Yao, Y.; Xu, L.; O'Brien, E.; Powers, A. S.; Ferry, V. E.; Alivisatos, A. P.; Nuzzo, R. G. Quantum Dot Luminescent Concentrator Cavity Exhibiting 30-fold Concentration. *ACS Photonics* **2015**, *2*, 1576−1583.
(19) Goldschmidt, J. C.; Peters, M.; Gutmann, J.; Steidl, L.; Zentel, R.; Bläsi, B.; Hermle, M. Increasing fluorescent concentrator light collection efficiency by restricting the angular emission characteristic of the incorporated luminescent material: the 'Nano-Fluko' concept. *Proc. SPIE* **2010**, *7725*, 77250S-77250S−11.
(20) Rau, U.; Einsele, F.; Glaeser, G. C. Efficiency limits of photovoltaic fluorescent collectors. *Appl. Phys. Lett.* **2005**, *87*, 171101.
(21) Goldschmidt, J. C.; Peters, M.; Prönneke, L.; Steidl, L.; Zentel, R.; Bläsi, B.; Gombert, A.; Glunz, S.; Willeke, G.; Rau, U. Theoretical and experimental analysis of photonic structures for fluorescent concentrators with increased efficiencies. *Phys. Status Solidi A* **2008**, *205*, 2811−2821.
(22) Peters, M.; Goldschmidt, J. C.; Löper, P.; Groß, B.; Üpping, J.; Dimroth, F.; Wehrspohn, R.; Bläsi, B. Spectrally-Selective Photonic Structures for PV Applications. *Energies* **2010**, *3*, 171−193.
(23) Huck, N. P. M.; Staupe, I.; Thirouard, A.; de Boer, D. K. G. Light Polarization by Cholesteric Layers. *Jpn. J. Appl. Phys.* **2003**, *42*, 5189.
(24) Jeong, S. M.; Sonoyama, K.; Takanishi, Y.; Ishikawa, K.; Takezoe, H.; Nishimura, S.; Suzaki, G.; Song, M. H. Optical cavity with a double-layered cholesteric liquid crystal mirror and its prospective application to solid state laser. *Appl. Phys. Lett.* **2006**, *89*, 241116.
(25) Jeong, S. M.; Takanishi, Y.; Ishikawa, K.; Nishimura, S.; Suzaki, G.; Takezoe, H. Sharply directed emission in microcavity organic light-emitting diodes with a cholesteric liquid crystal film. *Opt. Commun.* **2007**, *273*, 167−172.
(26) de Boer, D. K. G.; Lin, C.-W.; Giesbers, M. P.; Cornelissen, H. J.; Debije, M. G.; Verbunt, P. P. C.; Broer, D. J. Polarization-independent filters for luminescent solar concentrators. *Appl. Phys. Lett.* **2011**, *98*, 021111.
(27) Ng, H. M.; Moustakas, T. D.; Chu, S. N. G. High reflectivity and broad bandwidth AlN/GaN distributed Bragg reflectors grown by molecular-beam epitaxy. *Appl. Phys. Lett.* **2000**, *76*, 2818−2820.
(28) Wu, Z.; Lee, D.; Rubner, M. F.; Cohen, R. E. Structural Color in Porous, Superhydrophilic, and Self-Cleaning SiO_2/TiO_2 Bragg Stacks. *Small* **2007**, *3*, 1445−1451.
(29) Colodrero, S.; Ocaña, M.; Míguez, H. Nanoparticle-Based One-Dimensional Photonic Crystals. *Langmuir* **2008**, *24*, 4430−4434.
(30) Gonzalez-Garcia, L.; Lozano, G.; Barranco, A.; Miguez, H.; Gonzalez-Elipe, A. R. TiO_2-SiO_2 one-dimensional photonic crystals of controlled porosity by glancing angle physical vapour deposition. *J. Mater. Chem.* **2010**, *20*, 6408−6412.
(31) Gunning, W. J.; Hall, R. L.; Woodberry, F. J.; Southwell, W. H.; Gluck, N. S. Codeposition of continuous composition rugate filters. *Appl. Opt.* **1989**, *28*, 2945−2948.
(32) Abu-Safia, H. A.; Al-Sharif, A. I.; Abu Aljarayesh, I. O. Rugate filter sidelobe suppression using half-apodization. *Appl. Opt.* **1993**, *32*, 4831−4835.
(33) Lee, C.-C.; Tang, C.-J.; Wu, J.-Y. Rugate filter made with composite thin films by ion-beam sputtering. *Appl. Opt.* **2006**, *45*, 1333−1337.
(34) Nolte, A. J.; Rubner, M. F.; Cohen, R. E. Creating Effective Refractive Index Gradients within Polyelectrolyte Multilayer Films: Molecularly Assembled Rugate Filters. *Langmuir* **2004**, *20*, 3304−3310.
(35) Lorenzo, E.; Oton, C. J.; Capuj, N. E.; Ghulinyan, M.; Navarro-Urrios, D.; Gaburro, Z.; Pavesi, L. Porous silicon-based rugate filters. *Appl. Opt.* **2005**, *44*, 5415−5421.
(36) Kosten, E. D.; Kayes, B. M.; Atwater, H. A. Experimental demonstration of enhanced photon recycling in angle-restricted GaAs solar cells. *Energy Environ. Sci.* **2014**, *7*, 1907−1912.
(37) de Boer, D. K. G. Optimizing wavelength-selective filters for luminescent solar concentrators. *Proc. SPIE* **2010**, *7725*, 77250Q-77250Q−9.
(38) Goldschmidt, J. C.; Peters, M.; Bösch, A.; Helmers, H.; Dimroth, F.; Glunz, S. W.; Willeke, G. Increasing the efficiency of fluorescent concentrator systems. *Sol. Energy Mater. Sol. Cells* **2009**, *93*, 176−182.
(39) Slooff, L. H.; Burgers, A. R.; Debije, M. G. Reduction of escape cone losses in luminescent solar concentrators with cholesteric mirrors. *Proc. SPIE* **2008**, *7043*, 704306−7.
(40) Debije, M. G.; Van, M.-P.; Verbunt, P. P. C.; Kastelijn, M. J.; van der Blom, R. H. L.; Broer, D. J.; Bastiaansen, C. W. M. Effect on the output of a luminescent solar concentrator on application of organic wavelength-selective mirrors. *Appl. Opt.* **2010**, *49*, 745−751.
(41) Puzzo, D. P.; Bonifacio, L. D.; Oreopoulos, J.; Yip, C. M.; Manners, I.; Ozin, G. A. Color from colorless nanomaterials: Bragg reflectors made of nanoparticles. *J. Mater. Chem.* **2009**, *19*, 3500−3506.
(42) Yao, Y.; Brueckner, E.; Li, L.; Nuzzo, R. Fabrication and assembly of ultrathin high-efficiency silicon solar microcells integrating electrical passivation and anti-reflection coatings. *Energy Environ. Sci.* **2013**, *6*, 3071−3079.
(43) Bomm, J.; Büchtemann, A.; Chatten, A. J.; Bose, R.; Farrell, D. J.; Chan, N. L. A.; Xiao, Y.; Slooff, L. H.; Meyer, T.; Meyer, A.; van Sark, W. G. J. H. M.; Koole, R. Fabrication and full characterization of state-of-the-art quantum dot luminescent solar concentrators. *Sol. Energy Mater. Sol. Cells* **2011**, *95*, 2087−2094.
(44) Fisher, M.; Zanella, M.; Farrell, D. J.; Manna, L.; Stavrinou, P.; Chatten, A. J. Luminescent Solar Concentrators Utilising Aligned CdSe/CdS Nanorods. *Photovoltaic Specialists Conference (PVSC), 2011 37th IEEE*; 2011, pp 000858−000863.

DOI: 10.1021/acsphotonics.5b00630
ACS Photonics 2016, 3, 278−285